

Cell bulging and extrusion in a three-dimensional bubbly vertex model for curved epithelial sheets

Oliver M. Drozdowski and Ulrich S. Schwarz*

*Institute for Theoretical Physics, BioQuant, and Max Planck School Matter to Life,
Heidelberg University, 69120 Heidelberg, Germany*

(Dated: November 12, 2024)

Cell extrusion is an essential mechanism for controlling cell density in epithelial tissues. Another essential element of epithelia is curvature, which is required to achieve complex shapes, like in the lung or intestine. Here we introduce a three-dimensional bubbly vertex model to study the interplay between extrusion and curvature. We find a generic cellular bulging instability at topological defects which is much stronger than for standard vertex models. To clarify the underlying mechanism, we analytically calculate the energy landscape for a single bulging cell in a mean field tissue. We find that extrusion is energetically preferred at topological defects due to a redistribution of Gaussian curvature into the defect. We show that it can be driven both by a decrease in apico-basal tension or by contractile line tensions. We also show that extrusion can be suppressed by luminal pressure and interfacial bending rigidity, allowing for additional control of this important process. Our theory suggests that epithelial curvature naturally leads to cell bulging and extrusion because the interfacial curvature of individual cells at the defects strongly amplifies buckling effected by tissue-scale topological defects in elastic sheets.

I. INTRODUCTION

Epithelial tissues are close-packed and sealed cell layers that form the barriers between different compartments in the body, for example in the lung or the intestine. In order to regulate their cell density, they have to achieve a balance between cell division and cell death. Recently it has become clear that both processes are strongly connected to mechanics: cells divide more if they are stretched by neighboring cells at low cell density, and they stop dividing and die if the epithelium becomes too crowded [1–3]. In order to make sure that dying cells leave the tissue without disrupting its barrier function, they are expelled by extrusion, which means they are squeezed out of the epithelium without the generation of any voids [4, 5]. Extrusion is especially prominent in the intestine, where the epithelium renews itself every 3-5 days [6]. Here cells proliferate in the crypt regions and then move in a constant stream to the tip of villi, where they are extruded [7]. The exact mechanisms of extrusion are not clear, but one important element seems to be the presence of specialized actin structures on the lateral and basal sides [3]. For flat model epithelia, it has been shown that cell extrusion occurs preferentially at topological defects in the nematic orientation field of the cells [8–10].

In general, cells in non-stratified epithelia tend to have hexagonal order, because this is the close-packed optimum in two dimensions, similar to the situation in sphere packings and foams. Hexagonal order is also dominant in curved epithelial sheets [11–14]. However, now some pentagonal defects are required to generate curvature [12]. Due to Euler’s polyhedron theorem, 12 pentagonal defects are required to achieve the topology of a sphere,

with the possibility of additional pentagonal-heptagonal pairs. Thus topological defects occur naturally in curved epithelia, while in flat cell layers, they arise rather a in stochastic manner from the movement of cells. Because epithelia are often curved due to their biological function, for example in the crypts and villi of the intestine, the question arises if they might use the naturally occurring topological defects to promote cell extrusion. While previous theoretical models have addressed such extrusion in a flat configuration focusing on fluid-like epithelia [15] or neglecting the three-dimensional nature of the problem [16], the coupling of curvature, defects, and shape instabilities has hardly been addressed before. Defects in such a setting have been linked to extrusion in flat epithelia on a substrate in phase field models of tissues [15] and to shape instabilities in vertex models [17], but the underlying mechanisms and their relation to curvature have not been addressed yet.

Recently, we have reported on a morphological instability at topological disclination defects in curved hexagonal epithelia in the three-dimensional vertex model (VM) [18]. This buckling instability arises because spherical epithelia are effectively elastic shells, similar to viral capsids [19, 20] or buckyballs [21], for which such an instability is known since the pioneering work by Seung and Nelson [22]. However, the standard VM does not consider that cells might adapt their own interfacial curvature to their mechanical environment, which must be the first step toward bulging and extrusion. Here we investigate this aspect by using the bubbly vertex model (BVM). In contrast to the normal VM, which describes multicellular systems with flat interfaces, in the BVM the interfaces are curved [23–25]. Such interfacial curvature leverages the three-dimensional nature of the cellular system and allows for different mechanisms than the usual VM-approach to epithelia. Here we show that the BVM for curved epithelial sheets naturally explains why and how

* Corresponding author: schwarz@thphys.uni-heidelberg.de

cells can extrude preferentially at topological defects.

We start in Section II by showing with computer simulations that the curved interfaces in the BVM strongly amplify the buckling at defects in curved sheets if compared to the standard VM with flat interfaces. To understand the underlying instability theoretically, we consider the representative case of a shell with icosahedral symmetry in which interfacial curvature leads to a significant lowering of a previously described icosahedral buckling threshold [18, 19, 22]. In Section III we develop a continuum description of a defect cell in a mean field tissue, which allows us to analytically understand the underlying instability. We find that the possibility of curved interfaces results in a local decrease of the saddle splay modulus, thus leading to localization of Gaussian curvature in the defect. This analytical model captures the numerical shapes of icosahedral vertex model shells. Generalizing it in Section IV to shells without such strong symmetry properties, allows us to generally formulate a model for cell extrusion at pentagonal and hexagonal cells in a curved epithelial sheet. We find that both lowering the apico-basal surface tension and a supracellular actin ring may initiate bulging, while only the former allows for a transition of a partially extruded geometry toward full extrusion. Our model predicts a lower energy barrier for extrusion at topological (pentagonal) defects. Further, we show that this tendency can be reduced by increasing luminal pressure or rigidifying cellular interfaces. We close in Section V with a discussion of our results, including the relation to experimental observations.

II. BUBBLY VERTEX MODEL AND BULGING INSTABILITY AT TOPOLOGICAL DEFECTS

A. Definition of bubbly vertex model (BVM)

For the description of tissue mechanics and shape, we adopt the usual tension-based approach. We start from the regular three-dimensional vertex model for epithelial monolayers in which individual cells are described as bounded volumes with one apical, one basal and multiple lateral faces as boundaries. While in the classical vertex model these boundary faces are assumed to be flat by triangulating them with a passive interpolation point [18, 26], we explicitly want to consider the effect of possible interface curvature on the mechanics and thus introduce the bubbly vertex model, in which the interfaces are allowed to curve.

Each cell i has one apical area $A_{a,i}$, one basal area $A_{b,i}$ and the integrated lateral area $A_{l,i}$, corresponding to the areas of the boundary faces. We assume the faces to have surface tensions $\Gamma_{(\cdot)}$, where we assume each cell to have the same surface tension for the apical, basal, and lateral faces. The total energy of the tissue is then described by

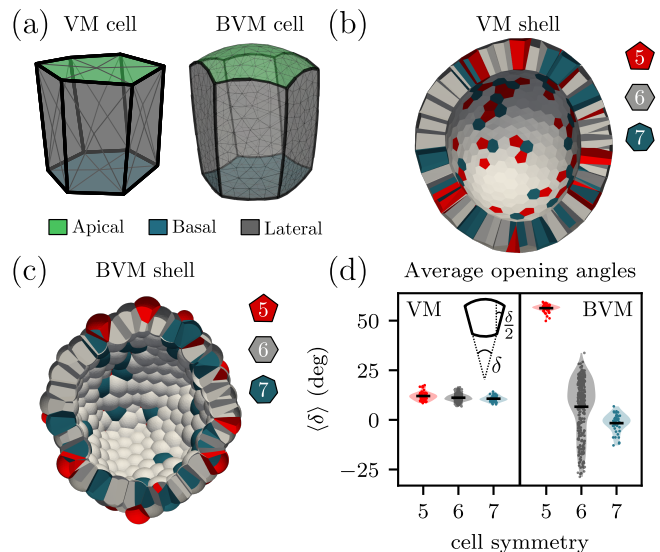


FIG. 1. Cell bulging at topological defects in the bubbly vertex model. (a) Schematic depiction of the vertex model (VM) representation of a cell with apical, basal and lateral faces via an interpolation point of the polygonal faces, and of the bubbly vertex model (BVM) representation with curved interfaces. (b) Spherical VM shell after energy minimization with random initialization of cell centers. (c) The same shell in the BVM after minimization in Surface Evolver. Cell symmetry is color-coded. (d) Opening angles of the cells by symmetry for the VM and BVM, where the half angle is determined for each lateral interface (inset) and then averaged over lateral interfaces. Violin plots show distribution with the horizontal line marking the average value. Shells with 400 cells and tensions $\Gamma_a = \Gamma_b = 0.9$, $\Gamma_l = 1$.

the sum of the individual surface area contributions

$$E = \sum_i \left(\Gamma_a A_{a,i} + \Gamma_b A_{b,i} + \frac{1}{2} \Gamma_l A_{l,i} \right), \quad (1)$$

where the factor 1/2 accounts for double counting. The apical and basal network topologies are identical, i.e., both apical and basal sides have the same number of adjacent apical and basal faces, respectively, and lateral faces are quadrilateral. We assume each cell to have a fixed volume V_{cell} . We non-dimensionalize the surface tension via Γ_l and the volume via V_{cell} , i.e., we set $\Gamma_l = 1$ and $V_{\text{cell}} = 1$.

Due to the viscoelastic behavior of the cell cortex [27, 28], we neglect elastic in-plane contributions of the interfaces, as these will relax over sufficiently long time scales. For now, we also do not consider a bending energy contribution [25], making use of the analogy to soap films, which are purely driven by surface tensions. This can be justified by the small thickness of the cortex, which will lead to small bending rigidities in the case of large interfacial tensions. We will relax this assumption later.

To differentiate between the model with and without membrane curvature, we call the former vertex model (VM) and the latter bubbly vertex model (BVM)

throughout the rest of this article. Fig. 1(a) schematically depicts the two model classes for one hexagonal cell.

B. Instability of luminal interfaces at topological defects

We consider a spherical epithelium with a randomized starting configuration. For simulations we use *Organoid-Chaste* [29], a custom-written package for Chaste [30] implementing a three-dimensional vertex model for monolayers, which was used in Ref. [18] and is described in Appendix A. Cell centers are created using the random sequential adsorption mechanism [31] and then a Voronoi tessellation on the sphere to determine cell shape. Using a rate of active topological T1-transitions which is slowly reduced to zero, the energy is minimized to obtain a spherical starting configuration. The resulting minimal energy configuration is shown in Fig. 1(b).

Next we minimized the energy in the BVM by using the VM configuration as starting configuration in the standard software *Surface Evolver* for energy minimization of surfaces under tension [32]. Again we minimize at constant cell volume and get the result shown in Fig. 1(c). As shown by the color code, for both the VM and the BVM, pentagons, hexagons and heptagons are distributed all over the surface. The spherical configuration necessitates curvature screening [33] through additional pairs of topological defects (pentagon-heptagon pairs) compared to an icosahedral configuration of a hexagonal lattice with 12 pentagons. While topological disclination defects indeed seem to be screened by the distribution of additional defect pairs in the VM, leading to an approximately spherical configuration, we observe an interesting instability in the BVM. Pentagonal cells tend to bulge outward, minimizing their luminal interfacial area, despite the fact that we do not observe a tissue-scale buckling instability. Fig. 1(d) demonstrates the dramatic difference between the two models: the opening angles of pentagonal cells are much larger in the BVM than in the VM, agreeing with the visual impression when comparing Figs. 1(b) and (c). In addition, we also see that the distribution of opening angles in the BVM is much broader with some cells even bending in the opposite direction. We conclude that the BVM allows for more adaption and variability in cell shape than the classical VM, with a particularly strong effect on the pentagonal defects.

C. Shift of icosahedral buckling threshold

The collapse of the luminal interface at pentagonal cells is reminiscent of the collapse observed earlier in the buckled icosahedral case in the VM for large apico-basal tensions Γ and thus cell heights [18]. In this case, a tissue-scale azimuthal stress from the pentagonal defect configuration is relaxed through conical buckling for large

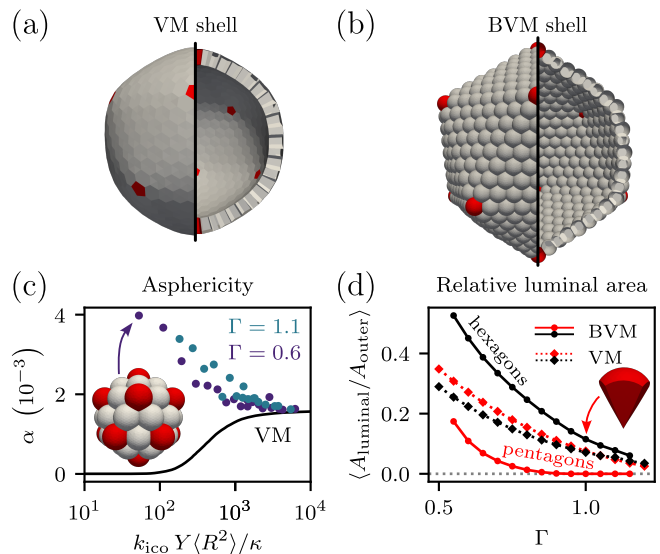


FIG. 2. Lowered buckling threshold for icosahedral instability in the bubbly vertex model (BVM) compared to the vertex model (VM). (a,b) Icosahedral shells with Caspar Klug indices $(8, 0)$ with tension $\Gamma = 0.6$ in the VM (a) and the BVM (b). (c) Asphericity $\alpha = \langle (R - \langle R \rangle)^2 \rangle / \langle R^2 \rangle$ of the cell centers in the BVM shell (symbols) and of the continuum curve describing the VM (taken from Refs. [18, 19]). Inset shows shell with size $(2, 0)$, $\Gamma = 0.6$. Radii are rescaled by the Young's modulus Y , bending rigidity κ and a nonlinearity correction k_{ico} , see Appendix B. (d) For a small shell (Caspar Klug indices $(2, 0)$) the average ratio of luminal and outer interfacial area in the BVM (solid) and VM (dashed). Inset shows pentagonal cell with collapsed luminal interface ($\Gamma = 1.0$). Pentagonal cells are shown in red.

tissues, an effect described before for elastic shells in general [22], leading to an icosahedral shape due to this effect occurring at the 12 pentagonal defects in the hexagonal tiling of the sphere. This system-scale instability is well-known from viral capsids [19, 20] and buckyballs [21]. On a single-cell scale, at these topological defects luminal interfaces can collapse due to the large necessary cellular opening angle at the icosahedral tips, quite similarly to what we observe in the BVM.

To be able to compare with these results for the VM, we now also consider spherical shells with icosahedral symmetry, following the Casper-Klug construction [34]. The Caspar-Klug indices (T_1, T_2) describe the steps in the underlying hexagonal lattice to go from one pentagonal defect cell to another with respect to lattice vectors with an opening angle of $\pi/3$. If we compare the results for the VM (Fig. 2 (a)) versus the results for the BVM (Fig. 2 (b)), we see that the buckling instability in the BVM is much stronger, for the same number of cells. It also occurs at smaller radii than the buckling instability in the VM, which only occurs for large system size. To quantify this effect, we measured the asphericity

$$\alpha = \langle (R - \langle R \rangle)^2 \rangle / \langle R^2 \rangle, \quad (2)$$

where R is the radial distance from the shell center and

$\langle \cdot \rangle$ the multicellular average. For the VM, this quantity has been shown before to follow a continuous curve as a function of the rescaled shell size (corresponding to the Föppl-von Kármán number) [18]. As shown in Fig. 2(c), the asphericity is much larger for small shells in the BVM compared to the VM. Details on the axis scaling are given in Appendix B.

We also find that the asphericities do not fall on one curve, but rather deviate from an average curve, which results from the broad distributions of hexagonal opening angles described above and therefore less regular structures. Similarly to the VM, we have a collapse of the luminal interface for larger Γ , which is much more pronounced in the BVM with a stronger deviation of the luminal-to-outer area ratios between pentagonal and hexagonal cells for small spheres, cf. Fig. 2 (d). Even shells as small as (2, 0), i.e. only one hexagonal cell between the pentagonal cells, show a big difference between pentagonal and hexagonal cells, and thus adopt a strongly icosahedral shape. We thus see that the buckling threshold is reduced to effectively one neighboring cell in the BVM, rendering the icosahedral tissue-scale instability much more relevant in the case of curved cellular interfaces in the BVM.

III. CONTINUUM THEORY OF A DEFECT CELL IN A MEAN-FIELD TISSUE

A. Parameterizing the defect cell

To understand the nature of the significant lowering of the icosahedral buckling threshold for the BVM compared to the VM, we now investigate the BVM in a continuum setting. We focus on the icosahedral tip and the conical instability to first develop the continuum model in a setting amenable to comparison to numerical simulations. At the site of the disclination defect we excise the continuous material and directly consider the energy of the pentagonal cell, following the description of the bubbly vertex model, cf. Eq. (1). Fig. 3(a) depicts the geometry we assume. At the center of the disc of material is the defect cell, which we consider first. We assume rotational symmetry and thus the cutout of the tissue is the base of a cone. The cell is allowed to bulge outward via interfacial curvature, which is captured by considering spherical caps at the apical and basal sides of the defect cell.

With the chosen parameterization we are able to describe different defect cell morphologies, i.e. a vertex model case with flat apical and basal interfaces, a bulged case with a collapsed interface, and an extruded case (Fig. 3(b)). Due to the pentagonal nature of the defect, we modify the conical shape to reflect the pentagonal structure by considering a pentagonal pyramid base, see Fig. 3(c). For this we introduce a geometrical factor ζ_{geom} , which relates the basal and apical polygonal edge lengths, b and a , respectively, to the areas such that

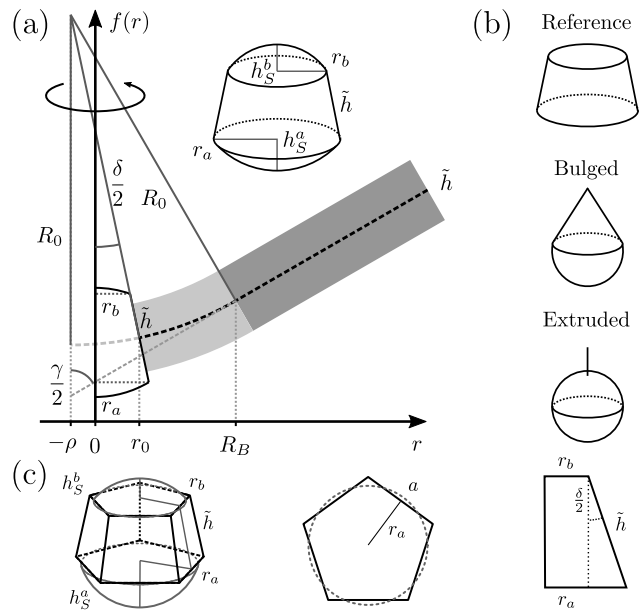


FIG. 3. Schematic depiction of the defect cell in a mean field tissue. (a) The tissue profile is shown as a radial function in cylindrical coordinates. At the center is the defect cell, which consists of a base of a cone with spherical caps on the apical and basal sides. This defect is surrounded by mean-field tissue that forms a spherical cap segment (light grey) and for larger distance a cone (dark grey). (b) The model can describe different defect cell geometries, namely, the vertex-model reference case ($h_S^a = h_S^b = 0$), a completely bulged case ($r_b = 0$, $\delta/2 > 0$) and a fully extruded case ($r_b = 0$, $\delta/2 = 0$). (c) For pentagonal cells we consider a geometrical correction, where we assume a pentagonal pyramid base with two spherical caps. The radii are chosen such that the area of the caps' disc bases match the pentagonal areas (center). and the slant height \tilde{h} is considered at the lateral faces' centers.

for the apical area $A_a = \zeta_{\text{geom}} a^2$ and similarly for the basal side. Additionally, we introduce η_{geom} , which relates the radius of a regular polygon's incircle $r_{a,b}$, i.e. the largest circle that fits into the regular polygon, to the edge length, e.g., for the apical side $r_a = \eta_{\text{geom}} a$.

For a bulged pentagonal cell we consider the pyramid base with apical/basal spherical caps. We assume the caps to have the same disc area as the apical/basal pentagons, neglecting the slight mismatch of the two different shapes, cf. Fig. 3(c). This is consistent with simulated cell shapes in the BVM as shown in Fig. 1(a). For the spherical caps we denote the base disc radii with $t_{(\cdot)}$. The cap's base area is $\pi t_{(\cdot)}^2$. This implies $\pi t_a^2 = \zeta_{\text{geom}} a^2$ for the apical side and analogously for the basal side. The radius of the apical spherical cap's base then relates to the edge length via $t_a = \sqrt{(\zeta_{\text{geom}}/\pi)} a$ and analogously for the basal side.

Henceforth we denote the side to which the tissue buckles (positive z) the basal side and the opposite side the apical one, as this corresponds to the sign of curvature at the villus tip in the small intestine. The opening an-

gle of the pyramid at the lateral face centers, $\delta/2$, the basal inradius r_b and the tissue height \tilde{h} define the base part. To consider the energy change due to extrusion and bulging, we define as the reference case the vertex model case, where the defect cell is not bulged and induces the same curvature as the tissue would. The spherical caps of the defect cell are uniquely defined by the basal and apical radii and the height of the caps $h_S^{a,b}$ (cf. Fig. 3).

The radius of curvature of the spherical caps $R_S^{a,b}$ depends on the pressure differences between the cell and the surrounding medium $\Delta P_{a,b}$ at the corresponding side via the Young-Laplace law

$$\Delta P_{a,b} = \frac{2\Gamma_{a,b}}{R_S^{a,b}}. \quad (3)$$

If we assume equal pressure differences, i.e., no pressure difference between the basal and apical medium, the radii are related via

$$\frac{R_S^a}{\Gamma_a} = \frac{R_S^b}{\Gamma_b}. \quad (4)$$

For the sake of simplicity we assume $\Gamma_a = \Gamma_b$ in this work, i.e., no apico-basal polarity. Using this relation, we express the basal cap height via the apical one, assuming that extrusion only occurs on the apical side and therefore choosing the smaller of two possible cap heights.

The volume of the cell then implicitly defines h_S^a via

$$1 = \frac{\tilde{h} \cos(\delta/2)}{3} \zeta_{\text{geom}} (a^2 + ab + b^2) + \frac{h_S^b}{6} (3\zeta_{\text{geom}} b^2 + \pi h_S^b{}^2) + \frac{h_S^a}{6} (3\zeta_{\text{geom}} a^2 + \pi h_S^a{}^2), \quad (5)$$

with the lateral (slant fraction) height \tilde{h} . The last two terms correspond to the spherical caps and vanish for the non-bulged reference cell as $h_S^b = h_S^a = 0$. The apical and basal sides are related to each other via the opening angle, $a = b + \sin(\delta/2)\tilde{h}/\eta_{\text{geom}}$, cf. Fig. 3(c). In the deformed cell, which we will now denote with a prime, the cap heights are then determined by b', δ' and \tilde{h} .

In a continuum approach we would not resolve the defect cell and the surrounding spherical cap with spherical radius R_0 would determine the opening angle, i.e., $\sin(\delta/2) = \eta_{\text{geom}} \left(1 + \frac{R_0 + \tilde{h}/2}{R_0 - \tilde{h}/2}\right) b/2R_0$. However, resolving the defect cell explicitly allows us to consider a vertex model later, which goes beyond this approximation, even if we do not allow for interfacial curvature.

With known cap heights we can write down the energy of the bubbly defect cell by adding the lateral surface energies and the surface energies of the spherical caps to obtain, where the cell is given by a regular n -gon (i.e. we

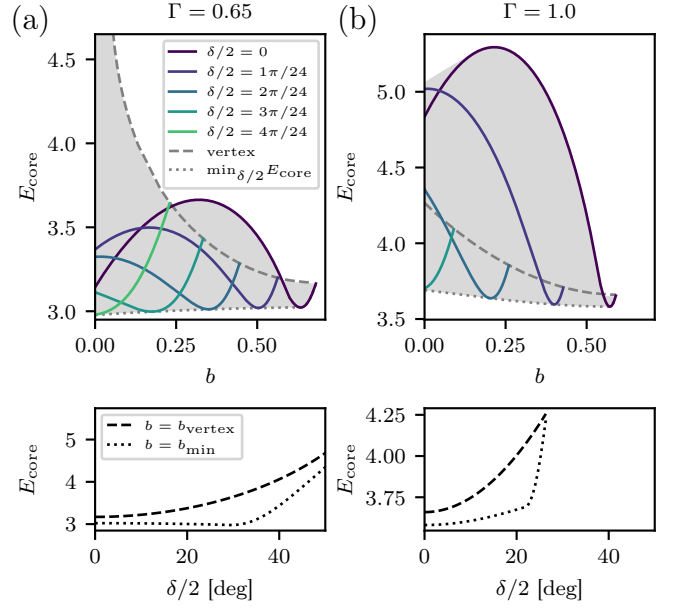


FIG. 4. The core energy for the different defect cell configurations for (a) small apical/basal surface tension Γ and (b) large Γ . The solid colored curves in the upper panels are the energies as a function of basal edge length b for fixed opening angles $\delta/2$. The curves end at the vertex line (dashed) at which b is maximal for the angle as such that the apical and basal faces do not bulge. All possible energies which can be reached with $\delta/2$ and b such that the volume constraint is fulfilled are shaded. The minimum line (dotted) indicates the minimal energy for given b . In the lower panels the vertex line and the minimum line are parametrized with $\delta/2$. The minimum line is obtained by finding the edge length b_{min} that minimizes E_{core} for a given $\delta/2$. We consider a pentagonal defect with equilibrium tissue height of the hexagonal vertex model, i.e., $\tilde{h} = 2^{1/3} 3^{-1/6} (2\Gamma)^{2/3}$.

first consider $n = 5$),

$$E_{\text{core}}^{\text{bulged}} = \Gamma_a (\zeta_{\text{geom}} a^2 + \pi h_S^a{}^2) + \Gamma_b (\zeta_{\text{geom}} b^2 + \pi h_S^b{}^2) + \frac{n\tilde{h}}{4} \left(2b + \frac{\tilde{h}}{\eta_{\text{geom}}} \sin(\delta/2) \right). \quad (6)$$

For a pentagonal defect we have $\zeta_{\text{geom}} = \sqrt{5(5 + 2\sqrt{5})}/4$ and $\eta_{\text{geom}} = 1/(2\sqrt{5 - \sqrt{20}})$. We assume that the lateral slant height of the pyramid base is the equilibrium height of the surrounding tissue \tilde{h} and thus the only two free parameters are b, δ . To describe the full tissue we additionally need the background curvature R_0 , which relates to the buckling radius R_B via the conical opening angle γ , cf. Fig. 3(a).

Fig. 4 shows the dimensionless core energy, Eq. (6), for different opening angles $\delta/2$ as a function of the basal edge length b for (a) $\Gamma = \Gamma_a = \Gamma_b = 0.65$ and (b) 1.0, respectively. Edge length b is bounded from above by the volume constraint in the unbulged vertex model

case with $h_S^b = h_S^a = 0$. For each angle the energy initially decreases if we decrease b with concomitant outward bulging (top panel), as the area to volume ratio decreases. For even smaller b the energy usually increases again, suggesting that a configuration with curved interfaces is always energetically more favorable.

Increasing the angle leads to an increase in the core energy in the vertex model case (cf. dashed line at which the curves end in the top panel) and shifts the minimum of the energy toward smaller b if we allow for bulging. If we compare the vertex model energy with the minimal energy in the bubbly vertex model for given opening angles (and thus surrounding tissue curvature), we find a smaller energy in the latter case, see lower panel.

Strikingly, as we increase $\delta/2$ and thus bend the defect cell, we either obtain a smaller increase of energy in the bubbly case compared to the vertex model ($\Gamma = 1.0$) or even an energy release ($\Gamma = 0.65$). As this is related to the bending rigidity, this drastically changes the behavior of the overall tissue. The potential to bulge outward therefore decreases the necessary bending energy in the defect core and can even lead to an energy release. This energy can then compensate for energy contributions in the surrounding tissue, allowing for a different equilibrium shape than in the two-dimensional elastic sheet. This effect explains the observed concentration of Gaussian curvature in the defect cell, as it is energetically cheaper to go into the buckled state for an icosahedral shell.

B. Deformation of the mean-field tissue

For the surrounding mean field tissue we assume that the inner radius of the inner tissue segment (cf. light grey part in Fig. 3(a)) corresponds to the polygonal in-radius of the defect cell, neglecting mismatch contributions here stemming from the shape difference between the cellular pentagonal mid-plane and circular cut-out. This inner cap segment is assumed to follow a circular arc with radius of curvature R_0 in cylindrical coordinates, cf. Fig. 3(a). An outer segment (cf. dark grey part) is assumed to be conical, in agreement to the result in moderately bent plates with a disclination defect.

We use the description as a moderately bent plate as derived in Ref. [18]. The energy change due to the defect deformation can then be split into different contributions. First, the bending energy will change, both for the mean and Gaussian curvature contributions, due to changes in the curvature radii and opening angles in the inner cap segment. Second, the stretching energy will change as the azimuthal strain stemming from the pentagonal defect can be relaxed through changes in the curvature. For simplicity we will neglect radial stretching contributions at the interfaces by considering stress free boundary conditions at the contact points of defect cell, cap segment and outer cone segment and at the outer edge of the cone, which we will justify numerically in the following.

Introducing the bending energy density e_{bending} and the stretching energy density e_{stretch} , the total energy of the tissue Ω then reads

$$E = \int_{\Omega} (e_{\text{bending}} + e_{\text{stretch}}) dS. \quad (7)$$

For the spherical topology of the tissue which we consider here, we consider the conical deformation of a disc with the pentagonal defect in the center, as this has been shown to capture the icosahedral instability of such a regular sphere [18, 19].

1. Bending energies

For the cap segment we consider the radial deflection function f with rotational symmetry

$$f(r) = R_0 - \sqrt{R_0^2 - (\rho + r)^2}, \quad (8)$$

where ρ is the radial offset due to the bulged defect cell, cf. Fig. 3. The bending energy density reads

$$e_{\text{bending}} = \frac{\kappa}{2} H^2 + \kappa_G K, \quad (9)$$

with bending rigidity κ , saddle splay modulus κ_G , (total) mean curvature $H = c + c'$, and Gauss curvature $K = cc'$ for principal curvatures c, c' . For the deflection function $f(r)$ the curvatures read

$$\begin{aligned} H(r) &= \frac{1}{r} \partial_r r \left(\frac{\partial_r f}{\sqrt{1 + (\partial_r f)^2}} \right) = \frac{2}{R_0} + \frac{\rho}{r R_0}, \\ K(r) &= \frac{\frac{1}{r} (\partial_r f) (\partial_r^2 f)}{(1 + (\partial_r f)^2)^2} = \frac{\rho + r}{r R_0^2}. \end{aligned} \quad (10)$$

With the area element, $dS = \sqrt{1 + f'^2} r d\phi dr$, the corresponding bending energy from mean curvature reads

$$\begin{aligned} \frac{E_{\text{bending}}^{\text{mean}}}{\kappa\pi} &= -\frac{4}{R_0} \sqrt{R_0^2 - (\rho + r)^2} - \frac{\rho^2}{\sqrt{R_0^2 - \rho^2}} \times \\ &\quad \text{artanh} \left(\frac{R_0^2 - \rho(\rho + r)}{(R_0^2 - \rho^2)^{1/2} (R_0^2 - (\rho + r)^2)^{1/2}} \right) \Bigg|_{r=r_0}^{r=R_B}. \end{aligned} \quad (11)$$

Note that for $\rho = r_0 = 0$ and small buckling radius R_B , i.e. small $|\nabla f|$ in the outer cone segment, the Taylor approximation in R_B scales quadratically, consistent with the approximation of the total energy with a flat disc as proposed by Seung and Nelson [22] for the flattened tip for the deformed shape around the defect. The first term in Eq. (11) arises from the spherical contribution of the mean curvature bending energy, cf. corresponding first term in the mean curvature in Eq. (10). The

second term, which is proportional to the squared radial offset ρ^2 , serves as a correction for reducing the radius of the circular segment in cylindrical coordinates, as we decrease the radius of curvature in the azimuthal direction via this offset. This term stems from the quadratic contribution of ρ^2 from the squared mean curvature, Eq. (10), in the bending energy.

The bending energy from Gaussian curvature only depends on the opening angle of the defect cell δ , as this modifies the solid angle covered by the cap segment, consistent with the Gauss-Bonnet theorem,

$$E_{\text{bending}}^{\text{Gauss}} = 2\pi\kappa_G [\cos(\delta/2) - \sin(\gamma/2)], \quad (12)$$

with tissue opening angle $\gamma/2$, cf. Fig. 3(a).

The conical part of the bending energy is unchanged to the respective result for large $|\nabla f|$ derived in Ref. [22]

$$E_{\text{cone}} = \frac{f_1}{(1 + f_1^2)^{1/2}} \pi\kappa \log(R/R_B), \quad (13)$$

with the total radius R , the buckling radius R_B , and the cone slope

$$f_1^{\text{cone}} = \left[\frac{1}{(1 - s/2\pi)^2} - 1 \right]^{1/2}. \quad (14)$$

This slope can be obtained by considering a cone where the base's circumference corresponds to the circumference of the corresponding flat disc segment with a wedge of angle s cut-out. In the case of a pentagonal defect this implies $s = 2\pi/6$.

2. Stretching energies

The stretching energy density reads

$$e_{\text{stretch}} = \frac{1}{2} (2\mu\varepsilon_{ij}^2 + \lambda\varepsilon_{kk}^2), \quad (15)$$

with two-dimensional Lamé coefficients μ and λ . To compute the stretching energy of the tissue we consider the in-plane deformation of a conically bent elastic sheet. Using polar coordinates (r, θ) , it is clear from symmetry that the azimuthal deformation function must be $u_\theta = q_s \theta r$, because we have a stretch of $q_s r$ if we denote with q_s the topological charge (i.e. the relative material fraction of necessary azimuthal stretching). For a pentagonal defect this means $q_s = s/2\pi = 1/6$, because 1/6 of the azimuthal circumference is removed.

Introducing the radial position function $w(r)$, the radial deformation is $u_r(r) = w(r) - r$ and the strains for a (moderately) bent plane [35] in polar coordinates are described by

$$\begin{aligned} \varepsilon_{rr} &= w'(r) - 1 + \frac{(f'(r))^2}{2}, \\ \varepsilon_{\theta\theta}(r) &= \frac{w(r) - r}{r} + q_s, \\ \varepsilon_{r\theta} &= 0, \end{aligned} \quad (16)$$

where the assumption of moderate bending yields a non-linear coupling term of the deflection function in the strain.

The energy containing both stretching and bending contributions, c.f. Eq. (7), hence constitutes a functional for w . The corresponding Euler-Lagrange equation for w is

$$\frac{w}{r} - w' - rw'' + \frac{2\mu}{2\mu + \lambda} \left(q_s - \frac{(f')^2}{2} \right) - rf'f'' = 0. \quad (17)$$

Determining the Euler-Lagrange equation for f from the sum of bending and stretching energy and considering a cone $f' = \text{const.}$ yields the identical result as obtained in Ref. [22], implying the bending energy $E = s\kappa \log(R/r_0)$ for some cut-off r_0 . For this result from Ref. [22] one uses $w(0) = 0$ and $\sigma_{rr}(R) = 0$ as boundary conditions.

We now want to take a different approach, however, and consider a ring of material with inner and outer radii r_0 and R_B , deflected with a known fixed slope $f' = f_1$. Introducing $\Delta s = q_s - f_1^2/2$, Eq. (17) is solved by

$$w(r) = \frac{\mu}{2\mu + \lambda} \Delta s r \log(r) + \frac{k_1}{r} + k_2 r, \quad (18)$$

with coefficients k_1 and k_2 , which are determined from the boundary conditions.

Note that the strains in Eq. (16) only consider the leading order terms in f' . To also allow for large f' , we observe that the azimuthal stretch in a cone is reduced such that for a circle at radius r the deformed radius becomes $r/\sqrt{1 + f_1^2}$. This results in the corrected radial strain $\varepsilon_{rr} = w'(r) - (1 + f_1^2)^{-1/2}$. Since we only consider a linear f , i.e. we neglect f'' , only the term corresponding to Δs changes in Eq. (17), implying that the solution is again Eq. (18), now with

$$\Delta s = q_s - \left(1 - \frac{1}{\sqrt{1 + f_1^2}} \right). \quad (19)$$

As boundary conditions we assume vanishing radial stresses at the inner and outer radii, i.e. at $r = r_0$ and $r = R_B$

$$\sigma_{rr}(r) = 2\mu\varepsilon_{rr}(r) + \lambda(\varepsilon_{rr}(r) + \varepsilon_{\theta\theta}(r)) = 0. \quad (20)$$

This boundary condition assumes that no radial (and thus total compressive) stresses act on the boundary of the cap segment and the conical part of the surrounding tissue. Comparing the cell height in VM simulations to the theoretical mean-field tissue height serves as an estimate for the compressive in-plane stress. The height difference from the mean-field height (cf. Appendix B) is shown in Fig. 5(a).

We see that our parameterization for the tissue shape seems reasonable in comparison to the VM shape: around the defect cell we have a ring of tissue which interpolates the opening angle of the cell and the tissue (corresponding to the light grey tissue in Fig. 3(a)), surrounded by

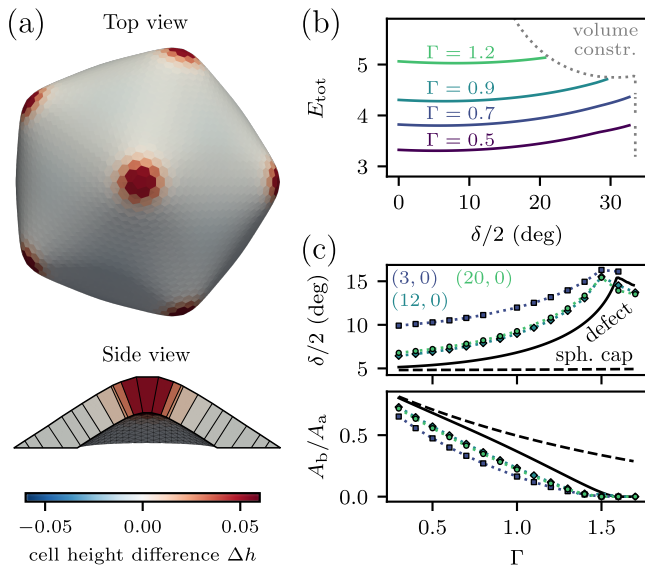


FIG. 5. Comparison of continuum model with vertex model simulations of icosahedral shells. (a) VM shell with Caspar-Klug size (20,0) and $\Gamma = 1.1$ with top view and side view cross-section. Color-coded is cell height difference from the mean-field VM height (cf. Eq. (B1)). (b) Total energy of the proposed full defect model as function of defect opening angle $\delta/2$ for different apical/basal surface tensions Γ . The dotted grey line indicates the angle boundary from the volume constraint. (c) Opening angles $\delta/2$ (top) and basal to apical face area ratios (bottom) for the different models. The defect model (solid) considers a defect in a mean-field tissue with the angle $\delta/2$ corresponding to the minimal energy configuration, cf. (a). The spherical cap model (dashed) corresponds to this energy under the assumption that $\delta/2$ matches the background curvature. The symbols indicate vertex model simulation results for different Caspar-Klug indices (T_1, T_2) .

a conically deformed background tissue (dark grey tissue in Fig. 3(a)). The height difference decays toward the boundary between the cap and the cone segments with a vanishing height difference (and thus stress) in the outer cone segment. Note, however, that our assumption on the defect cell height does not perfectly match the simulations. An additional coupling of tissue stress at the inner ring of the surrounding tissue and the defect cell's slant height could be introduced. We neglect this additional degree of freedom here in order to obtain a tractable model and as we obtain good agreement to simulations nonetheless.

After determining the coefficients $k_{1,2}$, we integrate the stretching energy to find

$$\frac{E_{\text{stretch}}}{\pi Y (1 + f_1^2)^{1/2}} = \frac{\Delta s^2}{8} (R_B^2 - r_0^2) - \frac{\Delta s^2}{2} \frac{R_B^2 r_0^2}{R_B^2 - r_0^2} \log^2 \left(\frac{R_B}{r_0} \right). \quad (21)$$

Coming back to the mean-field tissue, we now approximate the stretching energy in the cap segment (light grey

in Fig. 3(a)) by replacing it with a cone segment such that the slope matches the opening angle of the defect cell, $f_1 = \tan(\delta/2)$. If we consider the fully extruded case with $r_0 = 0$ and $\delta = 0$, we have the well-known analogous version of a flat disclination for large $|\nabla f|$ [22]. The corresponding approximation for small slopes has been used successfully in the description of viral capsids [19]. For the conical case, where the full Gaussian curvature is relaxed in the defect cell and $f_1 = f_1^{\text{cone}}$, we have $\delta/2 = \pi/6$ and $\Delta s = 0$, as it should. Our approximation thus serves as an interpolation between the two extreme limits of the stretching energy of a flat disclination (as used for viral capsids) and the solution for a cone, depending on the opening angle of the defect cell.

For the outer conical segment of the mean-field tissue (dark grey in Fig. 3(a)) we assume that it attains the conical shape and thus the stretching energy vanishes.

Finally, we can write down the full energy of the surrounding tissue as a sum of the contributions in Eqs. (11, 12, 13, 21), i.e.

$$E_{\text{tissue}} = E_{\text{bending}}^{\text{mean}} + E_{\text{bending}}^{\text{Gauss}} + E_{\text{cone}} + E_{\text{stretch}}. \quad (22)$$

C. Comparison to icosahedral vertex model shells

Due to the analytical tractability, icosahedral shells constitute a good test case. In Ref. [18] we have shown that their shape follows the described theory of moderately bent plates. Comparing it to simulations, we now show that the above parameterization and continuum theory are able to describe the shape of the pentagonal cell and of the surrounding tissue found in the VM.

The corresponding continuum model energy for this vertex model case consists of the core energy for a defect cell without bulging apical/basal membranes, i.e., with $h_S^a = 0 = h_S^b$, Eq. (6); the bending energy of both the cap segment, Eqs. (11, 12), and the outer cone region, Eq. (13); and the stretching energy in the cap, Eq. (21). For the resulting total energy E_{tot} we assume a large outer radius of the total disc R , such that area changes from deformations in the cone are negligible, and thus drop the term proportional to $\log(R)$ in Eq. (13), as we look at energy differences with respect to a reference state.

In the derivation of the mean field tissue (cf. Appendix B) lateral interface energies in the energy density are included by counting them half for the respective cell area (to avoid double counting). Here we now introduce a boundary energy term, which subtracts this lateral energy from the mean field tissue and adds half the pentagonal lattice energy of the defect. This lateral energy is present in full and should be considered completely, due to the explicit description of the defect cell. For the lateral contact between the defect and the tissue we thus subtract the lateral energy contribution which is implicitly given in the mean-field tissue boundary (with a circular cut-out) and replace it by the actual lateral energy contribution of the cell (with a pentagonal shape).

This energy reads

$$E_{\text{bdry}} = \frac{5\tilde{h}}{4} \left(2b + \frac{\tilde{h}}{\eta_{\text{geom}}} \sin(\delta/2) \right) - \pi r_0 \tilde{h} \quad (23)$$

and it is added to the total energy, i.e.

$$E_{\text{tot}} = E_{\text{core}} + E_{\text{bending}}^{\text{mean}} + E_{\text{bending}}^{\text{Gauss}} + E_{\text{cone}} + E_{\text{stretch}} + E_{\text{bdry}}. \quad (24)$$

For the elastic parameters and the bending rigidities of the mean-field tissues we use the mean-field values derived for the VM in Ref. [18], i.e. Eqs. (B2, B4) in Appendix B.

We found that for every $\delta/2$ and b the energy has a unique minimum as a function of the buckling radius R_B , or, equivalently, as a function of the radial cap curvature radius R_0 . We thus minimize the energy with respect to R_B to obtain the total energy as a function of the opening angle $\delta/2$ in the vertex model. Fig. 5(b) depicts the energies for different surface tensions Γ , where we observe a clear minimum. Note that for large Γ the volume constraint yields an upper bound for the possible opening angles. Our approach, the defect model, allows the defect to have an opening angle independently from the background tissue curvature. For comparison we also consider the case of the opening angle following the background curvature, i.e., $\delta/2$ is chosen such that it matches R_0 with $\rho = 0$, which we henceforth denote as the spherical cap model. The offset of the energies is a consequence of the neglect of the $\log(R)$ -term and results from the different cell number densities for different Γ .

In Fig. 5(c) we show the opening angle and the ratio of basal and apical interfacial areas in the minimal energy configuration. We see that the defect model predicts a strong increase of $\delta/2$ until $\Gamma \approx 1.4$ when the basal area completely collapses and the angle is determined by the volume constraint. The ratio of basal and apical areas, also shows this collapse. The symbols indicate vertex model simulations of spheres with different Caspar-Klug indices (T_1, T_2). Our defect model agrees well with the numerical vertex model data for large enough spheres and captures the shape of the defect much better than the model without the defect's ability to adopt a different opening radius as the surrounding tissue. Note that we do not have any fitting parameters, but rather derive the full model from the vertex model with only one free parameter, namely Γ . We thus conclude that the approach of considering a single defect cell in a mean field tissue captures the resulting shape better than an approach purely based on continuum theory, as exemplified by the comparison to the VM here.

IV. MECHANISMS OF CELL EXTRUSION

A. Extrusion of a bubbly defect cell in a mean-field vertex model tissue

After benchmarking our theoretical model by comparison with the unbulged classical vertex model, we return to the bubbly formulation of the vertex model. We now drop the assumption $h_S^b = 0 = h_S^a$ and consider a bulged defect cell in a vertex model mean-field tissue. In the following we will assume the mean-field tissue parameters to be from the classical (non-bubbly) VM, thus only allowing for bulging of the defect cell. In principle, however, mean-field parameters could be derived for the BVM in a similar fashion as for the VM, or could be taken from experimental measurements for the tissue properties.

Again, we consider the total energy as the sum of the contributions from the defect, the cap and the outer cone region. We now, however, consider the energy difference to a reference state to quantify the energy release due to bulging. For this we consider the energy difference ΔE from the vertex model case with minimal energy, which we obtain from the full defect model in this case, cf. Fig. 5.

As before, we find that for all configurations characterized by $\delta/2$ and b the energy has a unique minimum in the tissue buckling radius R_B . We assume this radius to be minimal for every defect cell shape and thus can describe all possible shapes by the variables $(\delta/2, b)$, which constitutes the configuration space. Both parameters are bounded from below by 0, where $(0, 0)$ is possible and corresponds to the fully extruded case, and from above by the volume constraint of the defect cell.

B. Pentagonal defect shape and extrusion for identical cell properties

Fig. 6 shows energy landscapes in configuration space for different surface tensions Γ . For now we assume identical cell properties, i.e. the tension in the defect cell matches the one of the surrounding tissue. We notice that, by bulging outward at the defect, the energy of the tissue can be reduced considerably in comparison to the classical vertex model reference case. For small Γ more energy can be released by bulging outward than for larger Γ . For $\Gamma > 0.5$ we observe that two minima form in the energy, one in the extruded case $(\delta/2, b) = (0, 0)$, and one in a bulged case with very small b . The energy minimum in extrusion is higher than the bulged one for larger Γ and an energy barrier has to be overcome from both the reference and the global minimum configuration to extrude the defect.

This effect is to be expected, because we have assumed that the bulged membrane has surface tension Γ and thus the fully extruded cell (surrounded by said membrane) will have a higher energy due to this larger surface tension. For $\Gamma < 0.5$ on the other hand we find that the

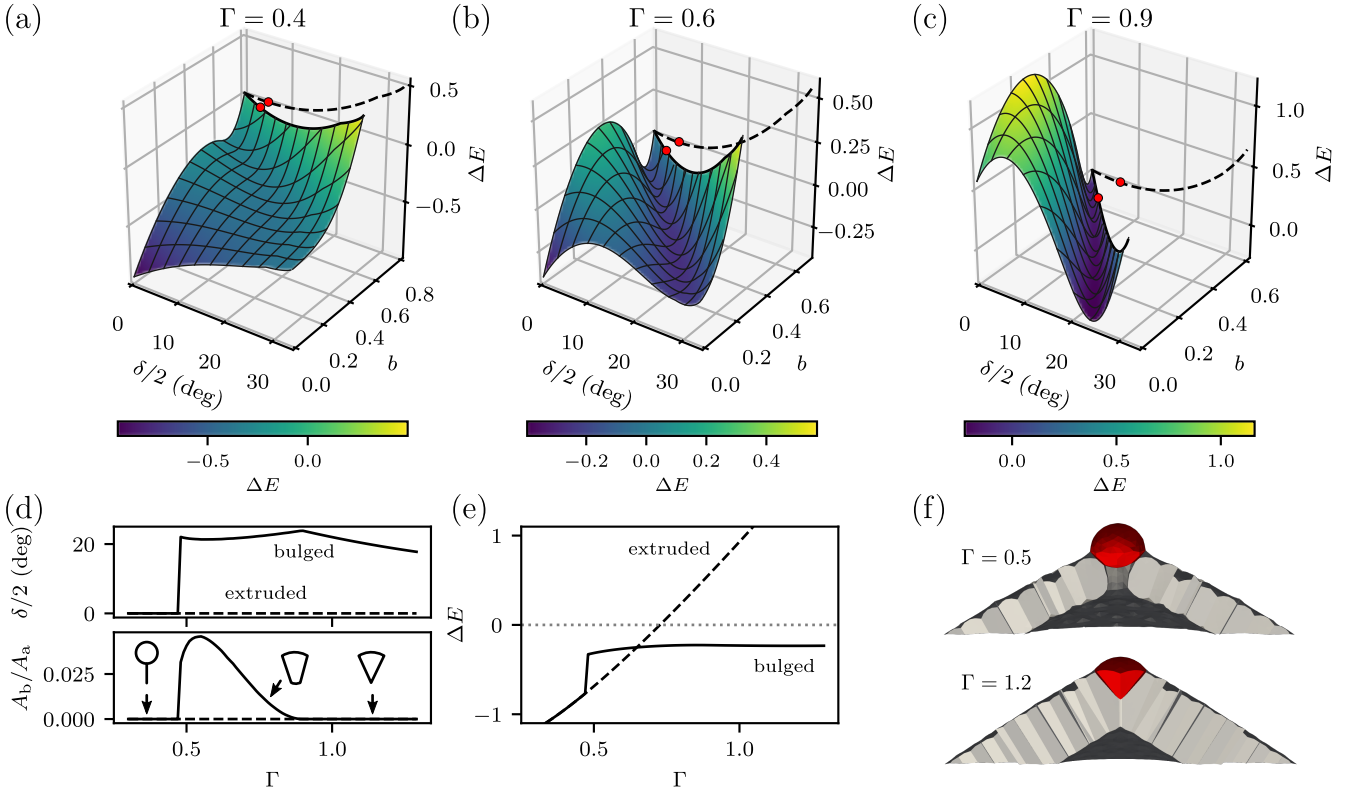


FIG. 6. Energy landscapes in configuration space and the resulting defect cell shapes. (a-c) Energy landscapes with coordinates $(\delta/2, b)$ for different surface tensions Γ . The black line marks the vertex model limit without bulging of the defect cell and the red circle marks the minimum in this limit. The dashed line is the projection onto the $(\Delta E, \delta/2)$ plane of this limit. The color codes the energy difference ΔE with respect to the reference energy, which is the vertex model minimum. The corners of the landscape at $(\delta/2, b) = (0, 0)$ and $(\delta_{\max}/2, 0)$ correspond to the extruded and maximally bent situations, respectively, cf. Fig. 3. (d) Defect opening angles $\delta/2$ (top) and basal vs. apical area ratio A_b/A_a (bottom) of the minimal energy configuration (solid), starting from the VM reference, and of the extruded configuration (dashed). (e) Corresponding energy differences from the VM reference ΔE . (f) For the bubbly vertex model with interfacial bending rigidity the defect cell is extruded for small apico-basal tension $\Gamma = 0.5$, and partially extruded for large tension $\Gamma = 1.2$. Shells of Caspar-Klug size $(T_1, T_2) = (12, 0)$ with bending rigidity $\kappa_{\text{if}} = 100$ in dimensionless units.

extruded case is minimal in energy and can directly be reached without passing over an energy barrier. The case $\Gamma = 0.5$ is special because it corresponds to cells with aspect ratio ≈ 1 , as the lateral energies only contribute half to the total energy, cf. Eq. (1), and thus energy costs for lateral and apico-basal interfaces do not differ. For $\Gamma < 0.5$ the lateral membrane is effectively more expensive than the apical membrane.

We now numerically determined the (local) minimal energy configurations for different Γ , starting from the VM reference state. Fig. 6(d,e) depicts the resulting minimal energy configurations. Above a critical tension Γ the luminal (basal) interface collapses but the angle remains finite, indicating a completely bulged state. The fully extruded state at $(\delta/2, b) = (0, 0)$ always represents a possible configuration, but its energy increases with Γ . Looking at the energy difference from the VM state, a configuration with interfacial curvature is always energetically more favorable, cf. Fig. 6(e). This is not surprising as the surface area can be minimized by the

cell becoming more spherical. The extruded case, on the other hand, requires more energy for large apico-basal tension, as we need to wrap the cell in the energetically (relatively) expensive apical interface. Lowering the tension allows for an energy release in the extruded case, which can become lower than in the bulged state. Note, however, that a bulged state persists beyond the point at which the extruded case is energetically more favorable and that an energy barrier exists in configuration space, which prevents the cell from being directly extruded from the reference VM configuration, cf. Fig. 6(b).

Considering icosahedral shells in the BVM and adding a bending rigidity across triangulation points of hexagonal cells' interfaces enables a numerical simulation similar to our continuum approach of a bubbly defect cell surrounded by VM cells. For this we consider an additional interfacial bending energy for each interface Ω_{if}

$$E_{\text{if}} = \frac{\kappa_{\text{if}}}{2} \int_{\Omega_{\text{if}}} H_{\text{if}}^2 dS, \quad (25)$$

with interfacial bending rigidity κ_{if} , and (total) mean curvature of the interface H_{if} . In this model we penalize interfacial curvature energetically.

Fig. 6(f) shows configurations of the defect cell in this BVM with bending rigidity for different apicobasal tensions Γ . For $\Gamma \leq 0.5$ we see that indeed the pentagonal cell is pushed out of the monolayer, only being attached because the lateral interfaces cannot be broken in the simulations. The luminal interfaces bend outward despite the energetic penalty to facilitate this extrusion process. For large Γ we indeed also find a completely bulged state, as predicted by the continuum model.

C. Pentagonal and hexagonal defects in shells with curvature screening and lower defect tension

We generalize our continuum description to spherical shells with curvature screening, as we have also seen an effect of topological defects in less structured monolayers, cf. Fig. 1. For this we assume the topological defect to only induce azimuthal strain locally around the defect. In simulations we see that pentagons with one neighboring ring of hexagonal cells exist in spherical shells due to the necessary excess topological charge (12 more pentagons than heptagons), cf. Fig. 1. Thus, we consider a defect cell, surrounded by a cap region with varying radius of curvature but fixed size (i.e. fixed buckling radius R_B), which in turn is surrounded by background tissue as depicted in Fig. 7(a). The background tissue is assumed to be mechanically relaxed and not considered in the following: the curvature is screened accordingly that a spherical configuration is obtained, cf. Fig. 1(b), and topological defects at most affect their neighbors. The in-radius for a hexagonal cell is

$$r_0^{\text{hex}} = \sqrt{\frac{1}{\tilde{h}\zeta_{\text{geom}}^{\text{tissue}}}} \eta_{\text{geom}}^{\text{tissue}} = 3^{-1/6} 2^{-2/3} (2\Gamma)^{-1/3}. \quad (26)$$

We now assume for the radius of the cap along the radial axis $R_B = 3r_0^{\text{hex}}$, i.e. one neighboring ring of cells. The background curvature radius R_{bg} only enters via the opening angle (similarly to the conical opening angle), i.e.

$$\pi/2 - \gamma/2 = \arcsin(R_B/R_{\text{bg}}). \quad (27)$$

For this configuration the total energy is now identical to the contributions from Eq. (24), but without the cone energy and with prescribed R_B and new angle $\gamma/2$, i.e.

$$E_{\text{tot}} = E_{\text{core}} + E_{\text{bending}}^{\text{mean}} + E_{\text{bending}}^{\text{Gauss}} + E_{\text{stretch}} + E_{\text{bdndry}}. \quad (28)$$

We now also want to consider extrusion of a hexagonal cell, for which we have no azimuthal stretching, i.e. a disclincity of $s = 0$ in Eq. (19), and consider $n = 6$ lateral faces. The geometric constants then read $\eta_{\text{geom}} = 3^{1/2}/2$ and $\zeta_{\text{geom}} = 3^{3/2}/2$. We have found that lower apicobasal tensions lead to extrusion, because the cell has to

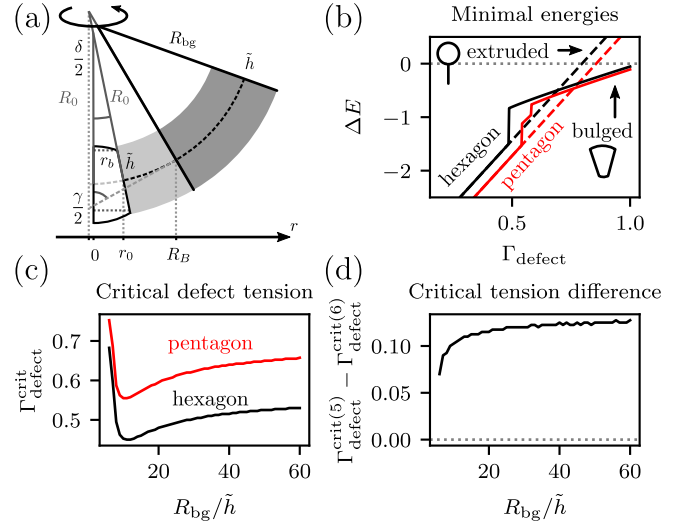


FIG. 7. Extrusion through lower defect tension in hexagons and pentagons. (a) Schematic depiction of defect in mean-field tissue with background curvature (radius R_{bg}). (b) The energy difference for configurations with different defect tensions Γ_{defect} from the VM case with identical defect tension $\Gamma_{\text{defect}} = \Gamma$. Solid line is local minimization from VM case, dashed line is extruded case. Red is pentagonal, black hexagonal defect cell. (c) Change of the critical defect tension $\Gamma_{\text{defect}}^{\text{crit}}$ at which the bulged state becomes unstable toward extrusion for different background radii R_{bg} . (d) Difference of critical tensions in pentagonal and hexagonal cells in (c). Parameters: $\Gamma = 0.9$; (b,c) $R_{\text{bg}}/\tilde{h} = 5$.

be completely engulfed by the apical interface in the extruded case. This suggests that one potential mechanism of extrusion is the lowering of apico-basal tension in the defect cell. Fig. 7(b) shows the energy differences from the VM reference for different defect tensions Γ_{defect} in a mean field tissue of tension $\Gamma = 0.9$. We see that pentagonal energies are generally smaller in deformed states due to the relaxation of azimuthal strain when localizing Gaussian curvature in the defect.

For both hexagons and pentagons we see that the extruded and bulged states become energetically more favorable as Γ_{defect} decreases. Below a critical tension $\Gamma_{\text{defect}}^{\text{crit}}$ the bulged state becomes unstable toward the extruded state. In Fig. 7(c) these critical tensions for pentagons and hexagons are plotted as functions of the background curvature radius R_{bg}/\tilde{h} . For a small radius the critical tension is high, implying that extrusion is easy. The reason for this is that the volume constraint does not allow for a full relaxation of the Gaussian curvature in the defect, because we have assumed that $\delta/2 < \pi/2 - \gamma/2$, i.e. the cap region cannot accommodate negative curvature. This leads to a less stable bulged state and thus earlier instability toward extrusion. For intermediate background radii the bulged state is able to stabilize by relaxing the remaining Gaussian curvature in the defect. Increasing the background radius further then leads to less stability of the bulged state, because the possible

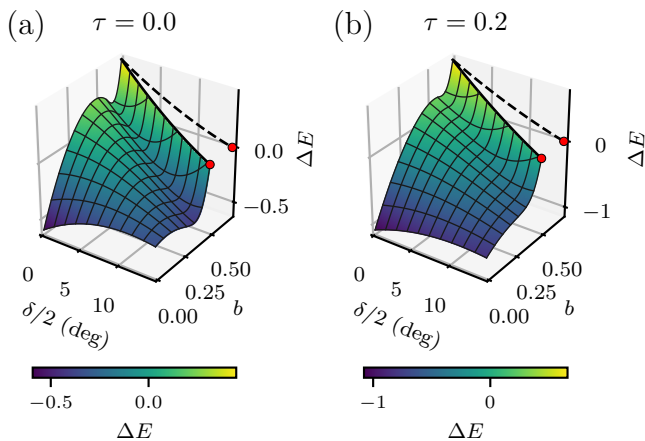


FIG. 8. Energy landscapes in configuration space for a pentagonal defect in a tissue with curvature screening and basal line tension τ . The cellular opening angle $\delta/2$ is bounded from above because of the maximum opening angle of the cap, see Fig. 7(a). Color-coding and lines as in Fig. 6(a-c). Parameters $\Gamma = 0.6$, $R_{\text{bg}}/\tilde{h} = 5$.

opening angle is small anyways.

In the pentagonal cell we see an intermediate state in Fig. 7(b): for intermediate tensions a local minimum of full bulging ($b = 0$, $\delta/2 > 0$) forms, which then becomes unstable toward the extruded case for lower tensions (cf. Fig. 7(a)). In general we see that for decreasing defect tensions in both pentagons and hexagons the energy landscape loses local minima corresponding to bulged states, as the extruded case becomes increasingly more energetically favorable.

Fig. 7(d) depicts the difference in the critical defect tensions of pentagons and hexagons, $\Gamma_{\text{defect}}^{\text{crit}(5)} - \Gamma_{\text{defect}}^{\text{crit}(6)}$. The necessary tension decrease for overcoming the energy barrier for extrusion in hexagons is approximately 10% of the total tension higher than for pentagonal cells. While this suggests pentagonal cells to be more prone to extrusion, it also does not constitute a difference large enough for other cellular processes to not be able to overcome the barrier for hexagons as well.

D. Effect of line tension on extrusion

Besides a reduction of apico-basal interfacial tension, another possible mechanism for extrusion are contractile actin structures pushing cells outward [3]. To consider such a process in our model, we add a line tension on the basal interface boundary, which effectively constitutes a contractile contribution along the basal interface edge. For a tension τ we thus have an energy

$$E_{\text{line}} = n \tau b. \quad (29)$$

Effectively this constitutes an additional b -dependent energy, which leads to a tilting of the energy landscape

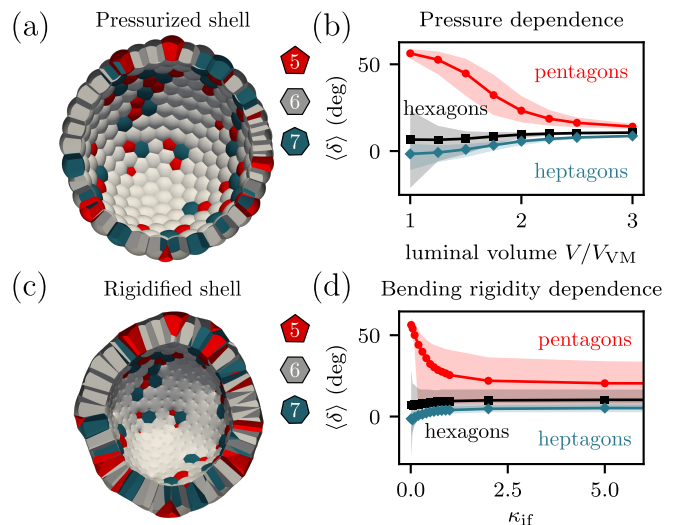


FIG. 9. Modulation of instability via luminal pressure and interfacial rigidity. (a) The shell from Fig. 1(c) is simulated with a luminal volume constraint $V/V_{\text{VM}} = 2$, corresponding to a luminal pressure. (b) Opening angles in the BVM for different volume constraints, where $V/V_{\text{VM}} \approx 1$ corresponds to the case without a luminal volume constraint. (c) Rigidified shell with interfacial bending rigidity $\kappa_{\text{if}} = 0.7$. (d) Opening angles for different κ_{if} , where $\kappa_{\text{if}} = 0$ is the BVM. Markers in (b,d) are average angles and shaded region shows 5% to 95% quantiles.

in configuration space, because in the case of curvature screening no R_0 minimization is performed. Fig. 8 displays such energy landscapes for pentagons ($n = 5$) for different line tensions τ . We do see that the tilting can destabilize bulged states. However, since at $b = 0$ the line tension does not contribute anymore, an energy barrier in the case of a transitioning from a bulged state with $b = 0$ to the extruded case, is not changed by the line tension. In light of partially extruded cells, such as in Fig. 6(f), this implies that an additional tuning of interfacial tensions (either lateral or apico-basal) is necessary to achieve full extrusion.

E. Instability modulation through luminal pressure and interface rigidity

To this point the effects of pressure and bending stiffness have been neglected. Fig. 9(a) shows a shell whose luminal volume was prescribed, corresponding to an internal luminal pressure. Internal pressure is able to unfold pentagonal defect cells. Contrary to the different opening angles for different cellular symmetries, cf. Fig. 1(c), pressure leads to convergence of the average opening angles of pentagons, hexagons, and heptagons as it increases, see Fig. 9(a). In addition, we also see that the distribution of opening angles in pressurized BVM shells is less broad, more closely resembling the classical VM case. This means that pressure can be used to

suppress the buckling instability caused by the surface tensions.

To highlight the role of interface curvature we added an interfacial bending energy to the BVM minimization, Eq. (25), with different interfacial bending rigidities κ_{if} . An exemplary shell shown in Fig. 9(c) displays less curved interfaces and also the defect cells are unfolded. Fig. 9(d) shows the opening angles, whose values quickly approach each other as κ_{if} is increased. However, contrary to luminal pressure, rigidifying the interfaces does not achieve a full convergence of the opening angles toward each other.

This shows that luminal pressures and rigid interfaces decrease the importance of topological defects in the BVM, which could serve as a mechanism for cells to achieve symmetry breaking and control extrusion and cell geometry. Moreover, including interfacial curvatures, as is necessary to describe some experimental systems, changes the importance of such defects drastically. In theoretical models of tissues it is thus important to reconsider the role of defects and the exact formulation of models, potentially rendering curvature energies, which are often neglected, central to capture single-cell behavior.

V. DISCUSSION

Here we have introduced the bubbly vertex model (BVM) for multicellular epithelial monolayers as a generalization of the standard vertex model (VM). In contrast to the VM, the BVM allows for curved interfaces, which are known to occur in flat epithelia and even more so in curved ones. Because curved epithelial sheets naturally have topological defects due to Euler's polyhedron theorem, we asked if cell bulging and extrusion might occur naturally at such defects. By comparing the BVM with the VM, we found that allowing for cell interface curvature dramatically lowers the conical buckling threshold around such defects.

In order to better understand the physical mechanism behind this observation, we developed a theory of a discrete defect cell in a mean-field tissue. This approach provides a mechanistic model for cell extrusion and it suggests that lowering the apico-basal tension in the cell to be extruded, and thus lowering the contractile forces and the mechanical stability of its cortex, provides a mechanism to extrude cells. Line tensions, as they could arise from supracellular actin structures, facilitate extrusion, but do not allow for the extrusion of partially extruded or fully bulged cells as they are observed in some experimental cases. Luminal pressures and interfacial rigidities directly reduce the influence of the topological defect on cell shape, which could serve as a mechanism for symmetry breaking in systems such as organoids.

Recently, intestinal organoids have emerged as a model system for curved epithelial sheets. Indeed partially extruded cells can be readily observed in such systems, cf. Fig. 10(a). Moreover one often observes varying cellu-

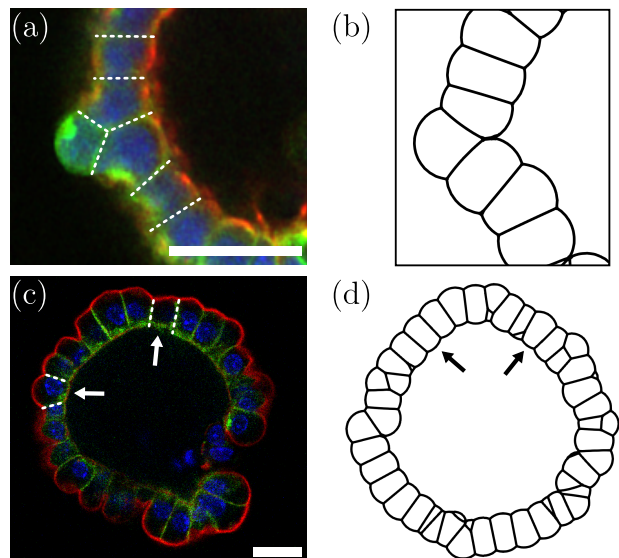


FIG. 10. Cell bulging as it is observed in mouse small intestine organoids and in the bubbly vertex model. (a) Organoid in which a single cell bulges outward into a partially extruded state. (b) Slice through a simulation of a spherical organoid with the bubbly vertex model with an apico-basal tension of $\Gamma = 0.9$ and a pentagonal defect tension of $\Gamma_{\text{defect}} = 0.65$, where a cell is partially extruded. (c) Organoid developing a bubbly shape with varying cellular opening angles (arrows). (d) Slice through a simulation of a spherical shell in the bubbly vertex model with $\Gamma = 0.9$. In (a,c) green is membrane (β -catenin), red is F-actin and blue nuclei. Microscopy data courtesy of Kim E. Boonekamp and Michael Boutros. Scale bars (a,c) $20 \mu\text{m}$.

lar opening angles, compare Fig. 10(c), which have been neglected and not found in standard formulations of the VM [36–38]. As shown in Fig. 10(b) and (d), the BVM can result in very similar shapes to the ones observed for the organoids, if the apico-basal tensions are reduced at pentagonal defects, as predicted by our theory.

Our model makes experimental predictions concerning a facilitated extrusion at pentagonal cells and a curvature dependence of the necessary tension decrease for extrusion. These predictions could be tested in the future in systems such as intestinal organoids in scaffolds [39], where the intestinal epithelium is reconstituted by considering an intestinal monolayer on a 3D substrate with similar shape as found in the intestine. In particular, in this approach cell extrusion has indeed been found to occur at the villus tips [39] and it could be used in the future to investigate our proposed dependence on the radius of background curvature. Intestinal organoids usually display an inverted sign of curvature compared to the villus domain in the intestine with the apical side pointing toward the lumen. Polarity reversed organoids, however, have the opposite apico-basal orientation and thus the correct curvature. They thus constitute another possible test system to study connections of single-cell shape and tissue curvature [40, 41], see an example image in

Fig. 10(c).

Our analytical model does not fully describe the morphology of partially extruded cells, because we neglected the relaxation of tilt in the neighboring cells. To better capture such intermediate morphologies of cell extrusion, as observed numerically in the BVM, and thus also obtain better predictions of stability, it is necessary to find a continuum description for these states. One possibility would be to introduce a continuous tilt field, to allow for deviations in the lateral configurations. It has been introduced before in the context of lipid membranes [42, 43], constituting a higher order correction in the continuum theory of bending. Together with the framework of a discrete cell in a mean-field tissue, which we presented here, it can serve as a starting point for further investigations of the coupling of single-cell and tissue-scale mechanics.

ACKNOWLEDGMENTS

We thank Kim E. Boonekamp and Michael Boutros for helpful discussions and for providing the microscopy data from Fig. 10. This research was conducted within the Max Planck School Matter to Life supported by the German Federal Ministry of Education and Research (BMBF) in collaboration with the Max Planck Society. USS is member of the Interdisciplinary Center for Scientific Computing (IWR) at Heidelberg.

Appendix A: Description of *OrganoidChaste*

The vertex model is implemented in *OrganoidChaste* [29], which is a package for Chaste [30]. Cells are polyhedra with apical, basal and lateral faces, which are described by nodes in 3D, cf. Fig. 1(a). As nodes of faces are not necessarily coplanar, we interpolate the interfaces by considering an average node for triangulation [18, 26]. To minimize the energy, Eq. (1), the force on node i is calculated based on the energy gradient with respect to the positions of node \mathbf{r}_i ,

$$\mathbf{F}_i = -\nabla_{\mathbf{r}_i} E. \quad (\text{A1})$$

Overdamped dynamics is assumed in the equation of motion of the nodes,

$$\frac{d}{dt} \mathbf{r}_i = \mathbf{F}_i, \quad (\text{A2})$$

where we assumed a mobility of one. This equation of motion is solved using Euler stepping. Volume conservation is achieved by projecting the forces on the manifold of volume conserving forces with an additional correction step [32].

Cells can perform neighbor exchanges, so-called T1 transitions, where we first form a protorosette and then in a next step create the new interface, following the approach suggested in Ref. [26]. We perform these ran-

domly with a probability given by a corresponding transition rate on the entire epithelium. This has been found to fluidize the 3D VM, allowing for a viscous relaxation of stresses [26]. In the minimization of the spherical epithelia a decreasing transition rate is taken, similarly to simulated annealing.

In order to solve the bubbly vertex model the configuration which is obtained in *OrganoidChaste* is exported to Surface Evolver [32], where the same energy, Eq. (1), is considered. However, the interpolation points of the triangulation are not longer averaged, allowing for interfacial curvature. If an interfacial bending rigidity is considered, then the mean curvature in Surface Evolver is calculated at triangulation points of the interfaces, which do not belong to the edges of three intersecting interfaces. This leads to small deviations at the corner triangles due to the neglect of a bending energy across the corresponding interface internal edge (cf. Fig. 9(c)), which decreases as the triangulation resolution is increased.

Appendix B: Continuum parameters for the mean field tissue

For the continuum description of the VM we consider a flat prototypical hexagonal cell without interfacial curvature, described by the VM energy, Eq. (1). Due to volume conservation, $V = 1$, we can relate the hexagonal edge length and the height. Minimizing the energy with respect to height yields equilibrium height [18]

$$h = 2^{1/3} 3^{-1/6} (\Gamma_a + \Gamma_b)^{2/3}. \quad (\text{B1})$$

To derive the elastic stretching parameters, in Ref. [18] a single-cell deformation is considered. For the same energy and hexagonal cells the Lamé coefficients read

$$2\mu = \lambda = (\Gamma_a + \Gamma_b), \quad (\text{B2})$$

which implies for the 2D Young's modulus and Poisson ratio

$$Y = \frac{4\mu(\mu + \lambda)}{2\mu + \lambda} = \frac{3}{2} (\Gamma_a + \Gamma_b), \quad (\text{B3})$$

$$\nu = \frac{\lambda}{2\mu + \lambda} = \frac{1}{2},$$

respectively. To derive the bending rigidity and saddle splay modulus, a curved cell is considered in Ref. [18] and the energy change as function of the cellular curvature for small curvatures is determined to find

$$\kappa = \frac{9}{8} \frac{1.26}{2^{1/3} 3^{4/3}} (\Gamma_a + \Gamma_b)^{1/3}, \quad (\text{B4})$$

$$\kappa_G = \left[\frac{(\Gamma_a + \Gamma_b)^2}{2} + \frac{3}{2} - \frac{9}{4} 1.26 \right] \frac{(\Gamma_a + \Gamma_b)^{1/3}}{2^{1/3} 3^{4/3}}.$$

In Ref. [18] it has been shown that the VM does not perfectly follow linear elasticity and that the stretching

moduli are functions of the strains. Thus a nonlinearity correction for the icosahedral instability is necessary

when considering the continuum limit of the VM, i.e. $k_{\text{ico}} = 1/2$.

-
- [1] G. T. Eisenhoffer, P. D. Loftus, M. Yoshigi, H. Otsuna, C.-B. Chien, P. A. Morcos, and J. Rosenblatt, *Nature* **484**, 546 (2012).
- [2] S. A. Gudipaty, J. Lindblom, P. D. Loftus, M. J. Redd, K. Edes, C. F. Davey, V. Krishnegowda, and J. Rosenblatt, *Nature* **543**, 118 (2017).
- [3] S. A. Gudipaty and J. Rosenblatt, *Semin. Cell Dev. Biol.* **67**, 132 (2017).
- [4] L. Kocgozlu, T. Saw, A. Le, I. Yow, M. Shagirov, E. Wong, R.-M. Mège, C. Lim, Y. Toyama, and B. Ladoux, *Curr. Biol.* **26**, 2942 (2016).
- [5] A. P. Le, J.-F. Rupprecht, R.-M. Mège, Y. Toyama, C. T. Lim, and B. Ladoux, *Nat. Commun.* **12**, 397 (2021).
- [6] L. G. van der Flier and H. Clevers, *Annu. Rev. Physiol.* **71**, 241 (2009).
- [7] C. Pérez-González, G. Ceada, M. Matejčić, and X. Trepast, *Curr. Opin. Genet. Dev.* **72**, 82 (2022).
- [8] T. B. Saw, A. Doostmohammadi, V. Nier, L. Kocgozlu, S. Thampi, Y. Toyama, P. Marcq, C. T. Lim, J. M. Yeomans, and B. Ladoux, *Nature* **544**, 212 (2017).
- [9] J. Fadul and J. Rosenblatt, *Curr. Opin. Cell Biol.* **54**, 66 (2018).
- [10] T. Chen, T. B. Saw, R.-M. Mège, and B. Ladoux, *J. Cell Sci.* **131**, jcs218156 (2018).
- [11] W. Tang, A. Das, A. F. Pegoraro, Y. L. Han, J. Huang, D. A. Roberts, H. Yang, J. J. Fredberg, D. N. Kotton, D. Bi, and M. Guo, *Nat. Phys.* **18**, 1371 (2022).
- [12] L. A. Hoffmann, L. N. Carenza, J. Eckert, and L. Giomi, *Sci. Adv.* **8**, eabk2712 (2022).
- [13] J. Eckert, B. Ladoux, R.-M. Mège, L. Giomi, and T. Schmidt, *Nat. Commun.* **14**, 5762 (2023).
- [14] J.-M. Armengol-Collado, L. N. Carenza, J. Eckert, D. Krommydas, and L. Giomi, *Nat. Phys.* **19**, 1773 (2023).
- [15] S. Monfared, G. Ravichandran, J. Andrade, and A. Doostmohammadi, *eLife* **12**, e82435 (2023).
- [16] C. Bielmeier, S. Alt, V. Weichselberger, M. La Fortezza, H. Harz, F. Jülicher, G. Salbreux, and A.-K. Classen, *Curr. Biol.* **26**, 563 (2016).
- [17] S. Okuda and K. Fujimoto, *Biophys. J.* **118**, 2549 (2020).
- [18] O. M. Drozdowski and U. S. Schwarz, *Phys. Rev. Res.* **6**, L022045 (2024).
- [19] J. Lidmar, L. Mirny, and D. R. Nelson, *Phys. Rev. E* **68**, 051910 (2003).
- [20] T. T. Nguyen, R. F. Bruinsma, and W. M. Gelbart, *Phys. Rev. E* **72**, 051923 (2005).
- [21] T. A. Witten and H. Li, *EPL* **23**, 51 (1993).
- [22] H. S. Seung and D. R. Nelson, *Phys. Rev. A* **38**, 1005 (1988).
- [23] Y. Ishimoto and Y. Morishita, *Phys. Rev. E* **90**, 052711 (2014).
- [24] A. Boromand, A. Signoriello, F. Ye, C. S. O’Hern, and M. D. Shattuck, *Phys. Rev. Lett.* **121**, 248003 (2018).
- [25] S. Runser, R. Vetter, and D. Iber, *Nat. Comput. Sci.* **4**, 299 (2024).
- [26] M. Krajnc, S. Dasgupta, P. Zihlerl, and J. Prost, *Phys. Rev. E* **98**, 022409 (2018).
- [27] A. Janshoff, *Biochem. Soc. Trans.* **49**, 2687 (2021).
- [28] A. Cordes, H. Witt, A. Gallemí-Pérez, B. Brückner, F. Grimm, M. Vache, T. Oswald, J. Bodenschatz, D. Flormann, F. Lautenschläger, M. Tarantola, and A. Janshoff, *Phys. Rev. Lett.* **125**, 068101 (2020).
- [29] O. M. Drozdowski and U. S. Schwarz, “OrganoidChaste: A three-dimensional vertex model for epithelial monolayers (WILL BE PUBLISHED UPON FINAL ACCEPTANCE),” <https://github.com/oliverdrozdowski/OrganoidChaste> (2024).
- [30] F. R. Cooper, R. E. Baker, M. O. Bernabeu, R. Bordas, L. Bowler, A. Bueno-Orovio, H. M. Byrne, V. Carapella, L. Cardone-Noott, J. Cooper, S. Dutta, B. D. Evans, A. G. Fletcher, J. A. Grogan, W. Guo, D. G. Harvey, M. Hendrix, D. Kay, J. Kursawe, P. K. Maini, B. McMillan, G. R. Mirams, J. M. Osborne, P. Pathmanathan, J. M. Pitt-Francis, M. Robinson, B. Rodriguez, R. J. Spiteri, and D. J. Gavaghan, *J. Open Source Softw.* **5**, 1848 (2020).
- [31] D. S. Roshal, K. Azzag, K. K. Fedorenko, S. B. Rochal, and S. Baghdigian, *Phys. Rev. E* **108**, 024404 (2023).
- [32] K. A. Brakke, *Exp. Math.* **1**, 141 (1992).
- [33] I. García-Aguilar, P. Fonda, and L. Giomi, *Phys. Rev. E* **101**, 063005 (2020).
- [34] D. L. D. Caspar and A. Klug, *Cold Spring Harb. Symp. Quant. Biol.* **27**, 1 (1962).
- [35] L. D. Landau and E. M. Lifshitz, *Theory of elasticity*, 2nd ed., Course of theoretical physics, Vol. 7 (Pergamon Press, Oxford, 1970).
- [36] Q. Yang, S.-L. Xue, C. J. Chan, M. Rempfler, D. Vischi, F. Maurer-Gutierrez, T. Hiiiragi, E. Hannezo, and P. Liberali, *Nat. Cell Biol.* **23**, 733 (2021).
- [37] E. Hannezo, J. Prost, and J.-F. Joanny, *Proc. Natl. Acad. Sci. U.S.A.* **111**, 27 (2014).
- [38] J. Rozman, M. Krajnc, and P. Zihlerl, *Nat. Commun.* **11**, 3805 (2020).
- [39] N. Gjorevski, M. Nikolaev, T. E. Brown, O. Mitrofanova, N. Brandenberg, F. W. DelRio, F. M. Yavitt, P. Liberali, K. S. Anseth, and M. P. Lutolf, *Science* **375**, eaaw9021 (2022).
- [40] J. Y. Co, M. Margalef-Català, X. Li, A. T. Mah, C. J. Kuo, D. M. Monack, and M. R. Amieva, *Cell Rep.* **26**, 2509 (2019).
- [41] J. Y. Co, M. Margalef-Català, D. M. Monack, and M. R. Amieva, *Nat. Protoc.* **16**, 5171 (2021).
- [42] M. Hamm and M. Kozlov, *EPJ E* **3**, 323 (2000).
- [43] M. M. Terzi and M. Deserno, *J. Chem. Phys.* **147**, 084702 (2017).